

We are IntechOpen, the world's leading publisher of Open Access books Built by scientists, for scientists

6,900

Open access books available

186,000

International authors and editors

200M

Downloads

Our authors are among the

154

Countries delivered to

TOP 1%

most cited scientists

12.2%

Contributors from top 500 universities



WEB OF SCIENCE™

Selection of our books indexed in the Book Citation Index
in Web of Science™ Core Collection (BKCI)

Interested in publishing with us?
Contact book.department@intechopen.com

Numbers displayed above are based on latest data collected.
For more information visit www.intechopen.com



High-Harmonic Generation

Kenichi L. Ishikawa

Photon Science Center, Graduate School of Engineering, University of Tokyo
Japan

1. Introduction

We present theoretical aspects of high-harmonic generation (HHG) in this chapter. Harmonic generation is a nonlinear optical process in which the frequency of laser light is converted into its integer multiples. Harmonics of very high orders are generated from atoms and molecules exposed to intense (usually near-infrared) laser fields. Surprisingly, the spectrum from this process, high-harmonic generation, consists of a plateau where the harmonic intensity is nearly constant over many orders and a sharp cutoff (see Fig. 5).

The maximal harmonic photon energy E_c is given by the cutoff law (Krause et al., 1992),

$$E_c = I_p + 3.17U_p, \quad (1)$$

where I_p is the ionization potential of the target atom, and $U_p[\text{eV}] = E_0^2 / 4\omega_0^2 = 9.337 \times 10^{-14} I$ [W/cm^2] (λ [μm])² the ponderomotive energy, with E_0 , I and λ being the strength, intensity and wavelength of the driving field, respectively. HHG has now been established as one of the best methods to produce ultrashort coherent light covering a wavelength range from the vacuum ultraviolet to the soft x-ray region. The development of HHG has opened new research areas such as attosecond science and nonlinear optics in the extreme ultraviolet (xuv) region.

Rather than by the perturbation theory found in standard textbooks of quantum mechanics, many features of HHG can be intuitively and even quantitatively explained in terms of electron rescattering trajectories which represent the semiclassical three-step model and the quantum-mechanical Lewenstein model. Remarkably, various predictions of the three-step model are supported by more elaborate direct solution of the time-dependent Schrödinger equation (TDSE). In this chapter, we describe these models of HHG (the three-step model, the Lewenstein model, and the TDSE).

Subsequently, we present the control of the intensity and emission timing of high harmonics by the addition of xuv pulses and its application for isolated attosecond pulse generation.

2. Model of high-harmonic generation

2.1 Three Step Model (TSM)

Many features of HHG can be intuitively and even quantitatively explained by the semiclassical three-step model (Fig. 1)(Krause et al., 1992; Schafer et al., 1993; Corkum, 1993). According to this model, in the first step, an electron is lifted to the continuum at the nuclear position with no kinetic energy through tunneling ionization (*ionization*). In the second step,

Source: Advances in Solid-State Lasers: Development and Applications, Book edited by: Mikhail Grishin, ISBN 978-953-7619-80-0, pp. 630, February 2010, INTECH, Croatia, downloaded from SCIYO.COM

the subsequent motion is governed classically by an oscillating electric field (*propagation*). In the third step, when the electron comes back to the nuclear position, occasionally, a harmonic, whose photon energy is equal to the sum of the electron kinetic energy and the ionization potential I_p , is emitted upon *recombination*. In this model, although the quantum mechanics is inherent in the ionization and recombination, the propagation is treated classically.

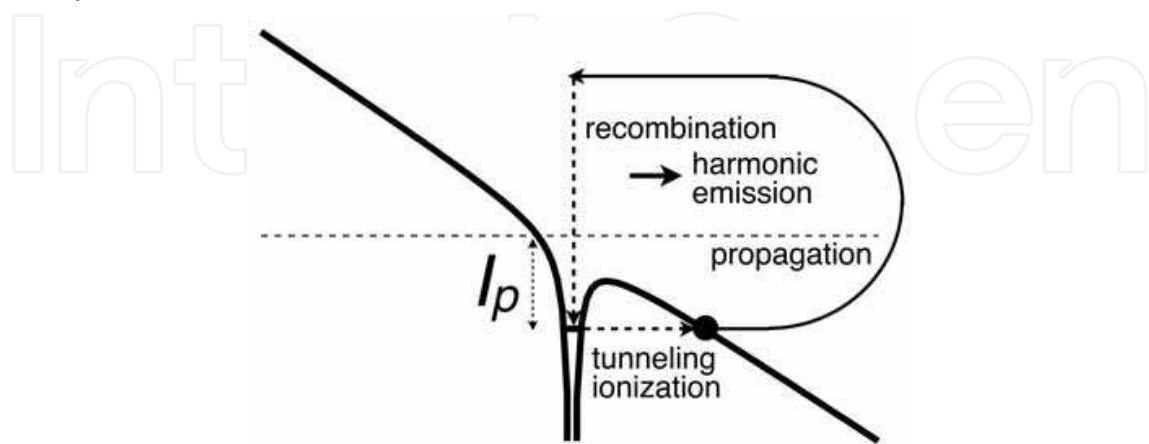


Fig. 1. Three step model of high-harmonic generation.

Let us consider that the laser electric field $E(t)$, linearly polarized in the z direction, is given by

$$E(t) = E_0 \cos \omega_0 t, \quad (2)$$

where E_0 and ω_0 denotes the field amplitude and frequency, respectively. If the electron is ejected at $t = t_i$, by solving the equation of motion for the electron position $z(t)$ with the initial conditions

$$z(t_i) = 0, \quad (3)$$

$$\dot{z}(t_i) = 0, \quad (4)$$

we obtain,

$$z(t) = \frac{E_0}{\omega_0^2} [(\cos \omega_0 t - \cos \omega_0 t_i) + (\omega_0 t - \omega_0 t_i) \sin \omega_0 t_i]. \quad (5)$$

It is convenient to introduce the phase $\theta \equiv \omega_0 t$. Then Equation 5 is rewritten as,

$$z(\theta) = \frac{E_0}{\omega_0^2} [(\cos \theta - \cos \theta_i) + (\theta - \theta_i) \sin \theta_i], \quad (6)$$

and we also obtain, for the kinetic energy E_{kin} ,

$$E_{kin}(\theta) = 2U_p (\sin \theta - \sin \theta_i)^2. \quad (7)$$

One obtains the time (phase) of recombination $t_r(\theta_r)$ as the roots of the equation $z(t) = 0$ ($z(\theta) = 0$). Then the energy of the photon emitted upon recombination is given by $E_{kin}(\theta_r) + I_p$.

Figure 2 shows $E_{kin}(\theta_r)/U_p$ as a function of phase of ionization θ_i and recombination θ_r for $0 < \theta_i < \pi$. The electron can be recombined only if $0 < \theta_i < \pi/2$; it flies away and never returns to the nuclear position if $\pi/2 < \theta_i < \pi$. $E_{kin}(\theta_r)$ takes the maximum value $3.17U_p$ at $\theta_i = 17^\circ$ and $\theta_r = 255^\circ$. This beautifully explains why the highest harmonic energy (cutoff) is given by $3.17U_p + I_p$. It should be noted that at the time of ionization the laser field, plotted in thin solid line, is close to its maximum, for which the tunneling ionization probability is high. Thus, harmonic generation is efficient even near the cutoff.

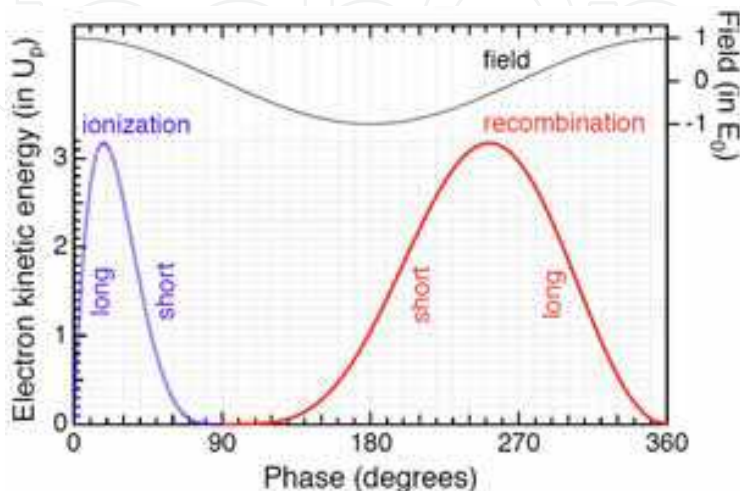


Fig. 2. Electron kinetic energy just before recombination normalized to the ponderomotive energy $E_{kin}(\theta_r)/U_p$ as a function of phase of ionization θ_i and recombination θ_r . The laser field normalized to the field amplitude $E(t)/E_0$ is also plotted in thin solid line (right axis).

For a given value of E_{kin} , we can view θ_i and θ_r as the solutions of the following coupled equations:

$$(\cos \theta_r - \cos \theta_i) + (\theta_r - \theta_i) \sin \theta_i = 0, \tag{8}$$

$$(\sin \theta_r - \sin \theta_i)^2 = \frac{E_{kin}}{2U_p} \tag{9}$$

The path $z(\theta)$ that the electron takes from $\theta = \theta_i$ to θ_r is called *trajectory*. We notice that there are two trajectories for a given kinetic energy below $3.17U_p$. $17^\circ < \theta_i < 90^\circ, 90^\circ < \theta_r < 255^\circ$ for the one trajectory, and $0^\circ < \theta_i < 17^\circ, 255^\circ < \theta_r < 360^\circ$ for the other. The former is called *short* trajectory, and the latter *long* trajectory.

If (θ_i, θ_r) is a pair of solutions of Equations 8 and 9, $(\theta_i + m\pi, \theta_r + m\pi)$ are also solutions, where m is an integer. If we denote $z(\theta)$ associated with m as $z_m(\theta)$, we find that $z_m(\theta) = (-1)^m z_{m=0}(\theta - m\pi)$. This implies that the harmonics are emitted each half cycle with an alternating phase, i.e., field direction in such a way that the harmonic field $E_h(t)$ can be expressed in the following form:

$$E_h(t) = \dots + F_h(t + 2\pi / \omega_0) - F_h(t + \pi / \omega_0) + F_h(t) - F_h(t - \pi / \omega_0) + F_h(t - 2\pi / \omega_0) - \dots \tag{10}$$

One can show that the Fourier transform of Equation 10 takes nonzero values only at odd multiples of ω_0 . This observation explains why the harmonic spectrum is composed of odd-order components.

In Fig. 3 we show an example of the harmonic field made up of the 9th, 11th, 13th, 15th, and 17th harmonic components. It indeed takes the form of Equation 10. In a similar manner, high harmonics are usually emitted as a train of bursts (*pulse train*) repeated each half cycle of the fundamental laser field. The harmonic field as in this figure was experimentally observed (Nabekawa et al., 2006).

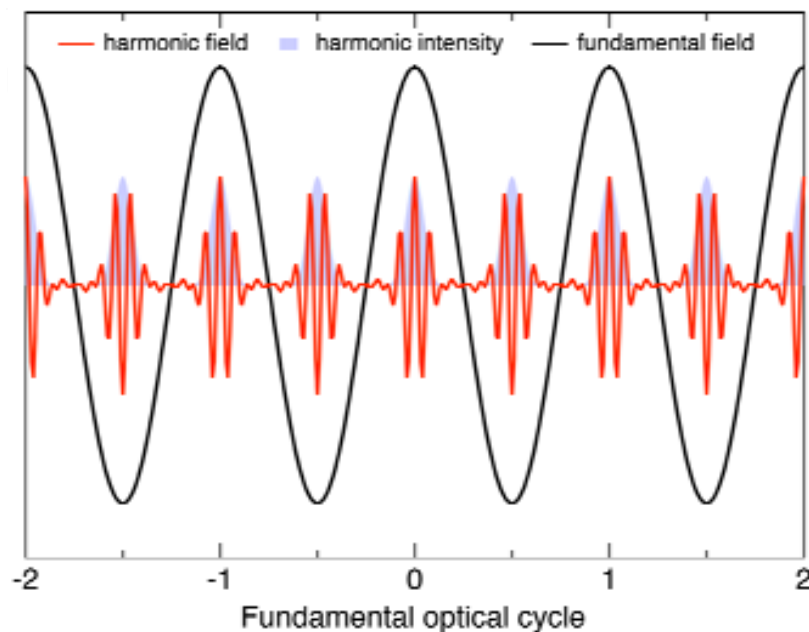


Fig. 3. Example of the harmonic field composed of harmonic orders 9, 11, 13, 15, and 17. The corresponding harmonic intensity and the fundamental field are also plotted.

2.2 Lewenstein model

The discussion of the propagation in the preceding subsection is entirely classical. Lewenstein et al. (Lewenstein et al., 1994) developed an analytical, quantum theory of HHG, called *Lewenstein model*. The interaction of an atom with a laser field $E(t)$, linearly polarized in the z direction, is described by the time-dependent Schrödinger equation (TDSE) in the length gauge,

$$i \frac{\partial \psi(r,t)}{\partial t} = \left[-\frac{1}{2} \nabla^2 + V(r) + zE(t) \right] \psi(r,t), \quad (11)$$

where $V(\mathbf{r})$ denotes the atomic potential. In order to enable analytical discussion, they introduced the following widely used assumptions (*strong-field approximation, SFA*):

- The contribution of all the excited bound states can be neglected.
- The effect of the atomic potential on the motion of the continuum electron can be neglected.
- The depletion of the ground state can be neglected.

Within this approximation, it can be shown (Lewenstein et al., 1994) that the time-dependent dipole moment $x(t) \equiv \langle \psi(\mathbf{r}, t) | z | \psi(\mathbf{r}, t) \rangle$ is given by,

$$x(t) = i \int_{-\infty}^t dt' \int d^3 \mathbf{p} d^* (\mathbf{p} + \mathbf{A}(t)) \cdot \exp[-iS(\mathbf{p}, t, t')] \cdot E(t') d(\mathbf{p} + \mathbf{A}(t')) + c.c., \quad (12)$$

where \mathbf{p} and $d(\mathbf{p})$ are the canonical momentum and the dipole transition matrix element, respectively, $\mathbf{A}(t) = -\int \mathbf{E}(t) dt$ denotes the vector potential, and $S(\mathbf{p}, t, t')$ the semiclassical action defined as,

$$S(\mathbf{p}, t, t') = \int_{t'}^t dt'' \left(\frac{[\mathbf{p} + \mathbf{A}(t'')]^2}{2} + I_p \right). \quad (13)$$

If we approximate the ground state by that of the hydrogenic atom,

$$\mathbf{d}(\mathbf{p}) = -\frac{i8\sqrt{2}(2I_p)^{5/4}}{\pi} \frac{\mathbf{p}}{(p^2 + 2I_p)^3}. \quad (14)$$

Alternatively, if we assume that the ground-state wave function has the form,

$$\psi(\mathbf{r}) = (\pi\Delta^2)^{-3/4} e^{-r^2/(2\Delta^2)}, \quad (15)$$

with $\Delta (\sim I_p^{-1})$ being the spatial width,

$$\mathbf{d}(\mathbf{p}) = i \left(\frac{\Delta^2}{\pi} \right)^{3/4} \Delta^2 \mathbf{p} e^{-\Delta^2 \mathbf{p}^2 / 2}. \quad (16)$$

In the spectral domain, Equation 12 is Fourier-transformed to,

$$\hat{x}(\omega_h) = i \int_{-\infty}^{\infty} dt \int_{-\infty}^t dt' \int d^3 \mathbf{p} d^* (\mathbf{p} + \mathbf{A}(t)) \cdot \exp[i\omega_h t - iS(\mathbf{p}, t, t')] \cdot E(t') d(\mathbf{p} + \mathbf{A}(t')) + \text{c.c.} \quad (17)$$

Equation 12 has a physical interpretation pertinent to the three-step model: $E(t')d(\mathbf{p} + \mathbf{A}(t'))$, $\exp[-iS(\mathbf{p}, t, t')]$, and $d^* (\mathbf{p} + \mathbf{A}(t))$ correspond to ionization at time t' , propagation from t' to t , and recombination at time t , respectively.

The evaluation of Equation 17 involves a five-dimensional integral over \mathbf{p} , t , and t' , i.e., the sum of the contributions from all the paths of the electron that is ejected and recombined at arbitrary time and position, which reminds us of Feynman's path-integral approach (Salières et al., 2001). Indeed, application of the saddle-point analysis (SPA) to the integral yields a simpler expression. The stationary conditions that the first derivatives of the exponent $\omega_h t - S(\mathbf{p}, t, t')$ with respect to \mathbf{p} , t , and t' are equal to zero lead to the saddle-point equations:

$$p(t - t') + \int_{t'}^t A(t'') dt'' = 0, \quad (18)$$

$$\frac{[p + A(t')]^2}{2} = -I_p, \quad (19)$$

$$\frac{[p + A(t)]^2}{2} = \omega_h - I_p, \quad (20)$$

Using the solutions (p_s, t_s, t'_s) , $\hat{x}(\omega_h)$ can be rewritten as a coherent superposition of quantum trajectories s :

$$\hat{x}(\omega_h) = \sum_s \left(\frac{\pi}{\varepsilon + \frac{i}{2}(t_s - t'_s)} \right)^{3/2} \frac{i2\pi}{\sqrt{\det S''(t, t')|_s}} d^*(p_s + A(t_s)) \times \exp[i\omega_h t_s - iS(p_s, t_s, t'_s)] E(t'_s) d(p_s + A(t'_s)), \quad (21)$$

where ε is an infinitesimal parameter, and

$$\det S''(t, t')|_s = \left(\frac{\partial^2 S}{\partial t \partial t'} \Big|_s \right)^2 - \frac{\partial^2 S}{\partial t^2} \Big|_s \frac{\partial^2 S}{\partial t'^2} \Big|_s, \quad (22)$$

$$\frac{\partial^2 S}{\partial t \partial t'} = \frac{(p + A(t))(p + A(t'))}{t - t'}, \quad (23)$$

$$\frac{\partial^2 S}{\partial t^2} = -\frac{2(\omega_h - I_p)}{t - t'} - E(t)(p + A(t)), \quad (24)$$

$$\frac{\partial^2 S}{\partial t'^2} = \frac{2I_p}{t - t'} + E(t')(p + A(t')), \quad (25)$$

The physical meaning of Equations 18-20 becomes clearer if we note that $p + A(t)$ is nothing but the kinetic momentum $v(t)$. Equation 18, rewritten as $\int_t^{t'} v(t'') dt'' = 0$, indicates that the electron appears in the continuum and is recombined at the same position (nuclear position). Equation 20, rewritten together with Equation 19 as $v(t)^2/2 - v(t')^2/2 = \omega_h$, means the energy conservation. The interpretation of Equation 19 is more complicated, since its right-hand side is negative, which implies that the solutions of the saddle-point equations are complex in general. The imaginary part of t' is usually interpreted as tunneling time (Lewenstein et al., 1994).

Let us consider again that the laser electric field is given by Equation 2 and introduce $\theta = \omega_0 t$ and $k = p\omega_0/E_0$. Then Equations 18-20 read as,

$$k = -\frac{\cos \theta - \cos \theta'}{\theta - \theta'}, \quad (26)$$

$$(k - \sin \theta')^2 = -\frac{I_p}{2U_p} = -\gamma^2, \quad (27)$$

$$(k - \sin \theta)^2 = \frac{\omega_h - I_p}{2U_p}, \quad (28)$$

where γ is called the *Keldysh parameter*. If we replace I_p and $\omega_h - I_p$ in these equations by zero and E_{kin} , respectively, we recover Equations 8 and 9 for the three-step model. Figure 4 displays the solutions (θ, θ') of these equations as a function of harmonic order. To make

our discussion concrete, we consider harmonics from an Ar atom ($I_p = 15.7596\text{eV}$) irradiated by a laser with a wavelength of 800 nm and an intensity of $1.6 \times 10^{14}\text{W/cm}^2$. The imaginary part of θ' (Fig. 4 (b)) corresponds to the tunneling time, as already mentioned. On the other hand, the imaginary part of θ is much smaller; that for the long trajectory, in particular, is nearly vanishing below the cutoff ($\approx 32\text{nd}$ order), which implies little contribution of tunneling to the recombination process. In Fig. 4 (a) are also plotted in thin dashed lines the trajectories from Fig. 2, obtained with the three-step model. We immediately notice that the Lewenstein model predicts a cutoff energy E_c ,

$$E_c = 3.17U_p + gI_p \quad (g \approx 1.3), \quad (29)$$

slightly higher than the three-step model (Lewenstein et al., 1994). This can be understood qualitatively by the fact that there is a finite distance between the nucleus and the tunnel exit (Fig. 1); the electron which has returned to the position of the tunnel exit is further accelerated till it reaches the nuclear position. Except for the difference in E_c , the trajectories from the TSM and the SPA (real part) are close to each other, though we see some discrepancy in the ionization time of the short trajectory. This suggests that the semi-classical three-step model is useful to predict and interpret the temporal structure of harmonic pulses, primarily determined by the recombination time, as we will see later.

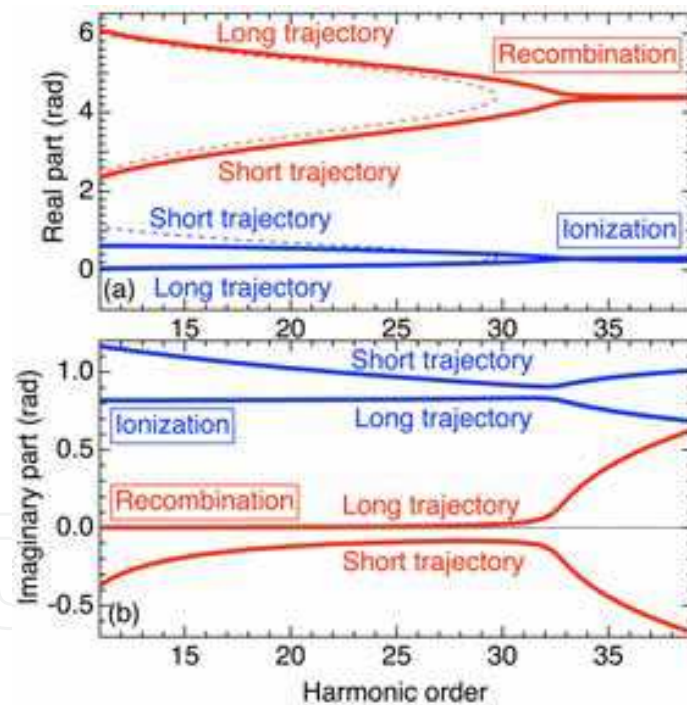


Fig. 4. (a) Real and (b) imaginary parts (radian) of the solutions θ (for recombination) and θ' (for ionization) of Equations 26-28 as a function of harmonic order ω_n/ω_0 . The value of $I_p = 15.7596\text{eV}$ is for Ar. The wavelength and intensity of the driving laser are 800 nm and $1.6 \times 10^{14}\text{W/cm}^2$. Thin dashed lines in panel (a) correspond to the three-step model.

2.3 Gaussian model

In the *Gaussian model*, we assume that the ground-state wave function has a form given by Equation 15. An appealing point of this model is that the dipole transition matrix element

also takes a Gaussian form (Equation 16) and that one can evaluate the integral with respect to momentum in Equation 12 analytically, without explicitly invoking the notion of quantum paths. Thus, we obtain the formula for the dipole moment $x(t)$ as,

$$x(t) = i\Delta^{-7} \int_{-\infty}^t (2C(t,t'))^{3/2} E(t') \times \{A(t)A(t') + C(t,t')[1 - D(t,t')(A(t) + A(t'))] + C^2(t,t')D^2(t,t')\} \times \exp\left(-i[I_p(t-t') + B(t,t')] - \frac{[A^2(t) + A^2(t')]\Delta^2 - C(t,t')D^2(t,t')}{2}\right) dt', \quad (30)$$

where $B(t, t')$, $C(t, t')$, and $D(t, t')$ are given by,

$$B(t,t') = \frac{1}{2} \int_{t'}^t dt'' A^2(t'') \quad , \quad (31)$$

$$C(t,t') = \frac{1}{2\Delta^2 + i(t-t')} \quad , \quad (32)$$

$$D(t,t') = [A(t) + A(t')]\Delta^2 + i \int_{t'}^t dt'' A(t'') \quad . \quad (33)$$

The Gaussian model is also useful when one wants to account for the effect of the initial spatial width of the wave function within the framework of the Lewenstein model (Ishikawa et al., 2009b).

2.4 Direct simulation of the time-dependent Schrödinger equation (TDSE)

The most straightforward way to investigate HHG based on the time-dependent Schrödinger equation 11 is to solve it numerically. Although such an idea might sound prohibitive at first, the TDSE simulations are indeed frequently used, with the rapid progress in computer technology. This approach provides us with exact numerical solutions, which are powerful especially when we face new phenomena for which we do not know a priori what kind of approximation is valid. We can also analyze the effects of the atomic Coulomb potential, which is not accounted for by the models in the preceding subsections. Here we briefly present the method developed by Kulander et al. (Kulander et al., 1992) for an atom initially in an s state. There are also other methods, such as the pseudo-spectral method (Tong & Chu, 1997) and those using the velocity gauge (Muller, 1999; Bauer & Koval, 2006).

Since we assume linear polarization in the z direction, the angular momentum selection rule tells us that the magnetic angular momentum remains $m = 0$. Then we can expand the wave function $\psi(\mathbf{r}, t)$ in spherical harmonics with $m = 0$,

$$\psi(\mathbf{r}, t) = \sum_l R_l(r, t) Y_l^0(\theta, \phi). \quad (34)$$

At this stage, the problem of three dimensions in space physically has been reduced to two dimensions. By discretizing the radial wave function $R_l(r, t)$ as $g_l^j = r_j R_l(r_j, t)$ with

$r_j = (j - \frac{1}{2})\Delta r$, where Δr is the grid spacing, we can derive the following equations for the temporal evolution (Kulander et al., 1992):

$$i \frac{\partial}{\partial t} g_i^j = -\frac{c_j g_i^{j+1} - 2d_j g_i^j + c_{j-1} g_i^{j-1}}{2(\Delta r)^2} + \left(\frac{l(l+1)}{2r_j^2} + V(r_j) \right) g_i^j \quad (35)$$

$$+ r_j E(t) (a_l g_{l+1}^j + a_{l-1} g_{l-1}^j) \\ = (H_0 g)_i^j + (H_l g)_i^j, \quad (36)$$

where the coefficients are given by,

$$c_j = \frac{j^2}{j^2 - 1/4}, \quad d_j = \frac{j^2 - j + 1/2}{j^2 - j + 1/4}, \quad a_l = \frac{l+1}{\sqrt{(2l+1)(2l+3)}}. \quad (37)$$

Here, in order to account for the boundary condition at the origin properly, the Euler-Lagrange equations with a Lagrange-type functional (Kulander et al., 1992; Koonin et al., 1977),

$$\mathcal{L} = \langle \psi | i\partial / \partial t - (H_0 + H_l(t)) | \psi \rangle, \quad (38)$$

has been discretized, instead of Equation 11 itself. c_j and d_j tend to unity for a large value of j , i.e., a large distance from the nucleus, with which the first term of the right-hand side of Equation 35 becomes an ordinary finite-difference expression. The operator H_0 corresponds to the atomic Hamiltonian and is diagonal in l , while H_l corresponds to the interaction Hamiltonian and couples the angular momentum l to the neighboring values $l \pm 1$.

Equations 35 and 36 can be integrated with respect to t by the *alternating direction implicit* (Peaceman-Rachford) scheme,

$$g_i^j(t + \Delta t) = [I + iH_0 t / 2]^{-1} [I + iH_l t / 2]^{-1} [I - iH_l t / 2] [I - iH_0 t / 2], \quad (39)$$

with Δt being the time step. This algorithm is accurate to the order of $\mathcal{O}(\Delta t^3)$, and approximately unitary. One can reduce the difference between the discretized and analytical wave function, by scaling the Coulomb potential by a few percent at the first grid point (Krause et al., 1992). We can obtain the harmonic spectrum by Fourier-transforming the dipole acceleration $\ddot{x}(t) = -\partial_i^2 \langle z(t) \rangle$, which in turn we calculate, employing the Ehrenfest theorem, through the relation $\ddot{x}(t) = \langle \psi(\mathbf{r}, t) | \cos \theta / r^2 - E(t) | \psi(\mathbf{r}, t) \rangle$ (Tong & Chu, 1997), where the second term can be dropped as it does not contribute to the HHG spectrum.

$V(r)$ is the bare Coulomb potential for a hydrogenic atom. Otherwise, we can employ a model potential (Muller & Kooiman, 1998) *within the single-active electron approximation* (SAE),

$$V(r) = -[1 + Ae^{-r} + (Z - 1 - A)e^{-Br}] / r, \quad (40)$$

where Z denotes the atomic number. Parameters A , and B are chosen in such a way that they faithfully reproduce the eigenenergies of the ground and the first excited states. One can account for nonzero azimuthal quantum numbers by replacing a_l by (Kulander et al., 1992),

$$a_l^m = \sqrt{\frac{(l+1)^2 - m^2}{(2l+1)(2l+3)}}. \quad (41)$$

In Fig. 5 we show an example of the calculated harmonic spectrum for a hydrogen atom irradiated by a Ti:Sapphire laser pulse with a wavelength of 800 nm ($\hbar\omega_0 = 1.55\text{eV}$) and a peak intensity of $1.6 \times 10^{14}\text{W/cm}^2$. The laser field $E(t)$ has a form of $E(t) = f(t) \sin\omega_0 t$, where the field envelope $f(t)$ corresponds to a 8-cycle flat-top pulse with a half-cycle turn-on and turn-off. We can see that the spectrum has peaks at odd harmonic orders, as is experimentally observed, and the cutoff energy predicted by the cutoff law.

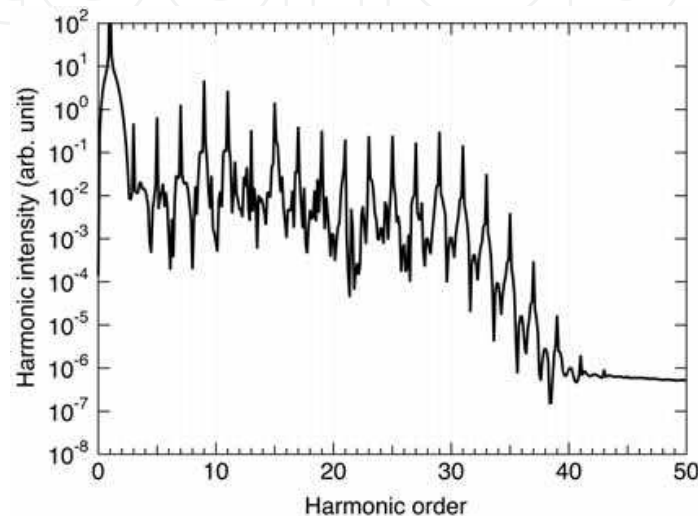


Fig. 5. HHG spectrum from a hydrogen atom, calculated with the Peaceman-Rachford method. See text for the laser parameters.

3. High-harmonic generation by an ultrashort laser pulse

Whereas in the previous section we considered the situation in which the laser has a constant intensity in time, virtually all the HHG experiments are performed with an ultrashort (a few to a few tens of fs) pulse. The state-of-the-art laser technology is approaching a single-cycle limit. The models in the preceding section can be applied to such situations without modification.

For completeness, the equations for the recombination time t and ionization time t' in the three-step model is obtained by replacing I_p in the right-hand side of Equation 19 by zero as follows:

$$-A(t')(t-t') + \int_{t'}^t A(t'') dt'' = 0, \quad (42)$$

$$\frac{[A(t) - A(t')]^2}{2} = \omega_h - I_p. \quad (43)$$

The canonical momentum is given by $p = -A(t')$.

In the Lewenstein model, any form of electric field $E(t)$ can be, through Fourier transform, expanded with sine waves, defined in the complex plane. Thus the saddle-point equations 18-20 can be solved at least numerically.

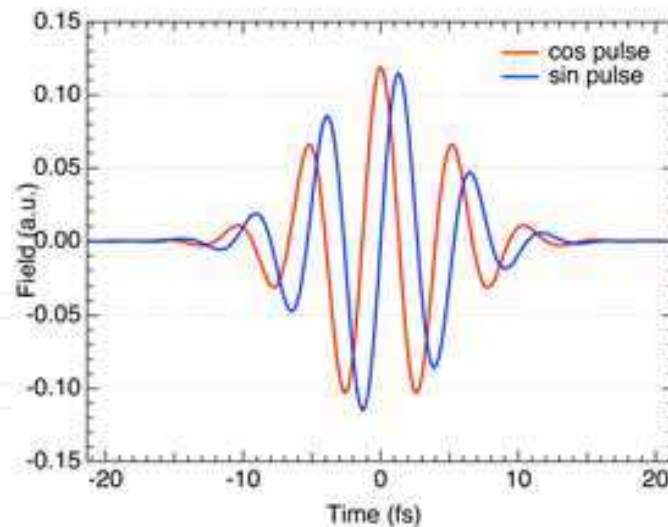


Fig. 6. Electric fields of cos and sin pulses.

In this subsection, let us consider HHG from a helium atom irradiated by an ultrashort laser pulse whose central wavelength is 800 nm, temporal profile is Gaussian with a full-width-at-half-maximum (FWHM) pulse duration $T_{1/2}$ of 8 fs (1.5 cycles), and peak intensity of $5 \times 10^{14} \text{W/cm}^2$. There are two particular forms of electric field, as shown in Fig. 6,

$$E(t) = f(t) \cos \omega_0 t \quad (\text{cos pulse}), \quad (44)$$

and,

$$E(t) = f(t) \sin \omega_0 t \quad (\text{sin pulse}), \quad (45)$$

where the field envelope $f(t)$ is given by,

$$f(t) = E_0 e^{-(2 \ln 2) t^2 / T_{1/2}^2}. \quad (46)$$

In general, when the field takes a form of,

$$E(t) = f(t) \cos(\omega_0 t + \phi_0), \quad (47)$$

ϕ_0 is called *carrier-envelope phase (CEP)*. The CEP is zero and $-\pi/2$ for cos and sin pulses, respectively.

3.1 Cos pulse

Figure 7 (a) displays the real part of the recombination (t) and ionization (t') times calculated with the saddle-point equations for the 1.5-cycle cos pulse. The recombination time from the three-step model, also shown in this figure, is close to the real part of the saddle-point solutions. By comparing this figure with the harmonic spectrum calculated with direct simulation of the TDSE (Fig. 7 (b)), we realize that the steps around 400 and 300 eV in the spectrum correspond to the cutoff of trajectory pairs C and D. Why does not a step (cutoff) for pair B appear? This is related to the field strength at time of ionization, indicated with vertical arrows in Fig. 7 (a). That for pair B (~ -5 fs) is smaller than those of pairs C (~ -2.5 fs) and D (~ 0 fs). Since the tunneling ionization rate (the first step of the three-step model) depends exponentially on intensity, the contribution from pair B is hidden by those from

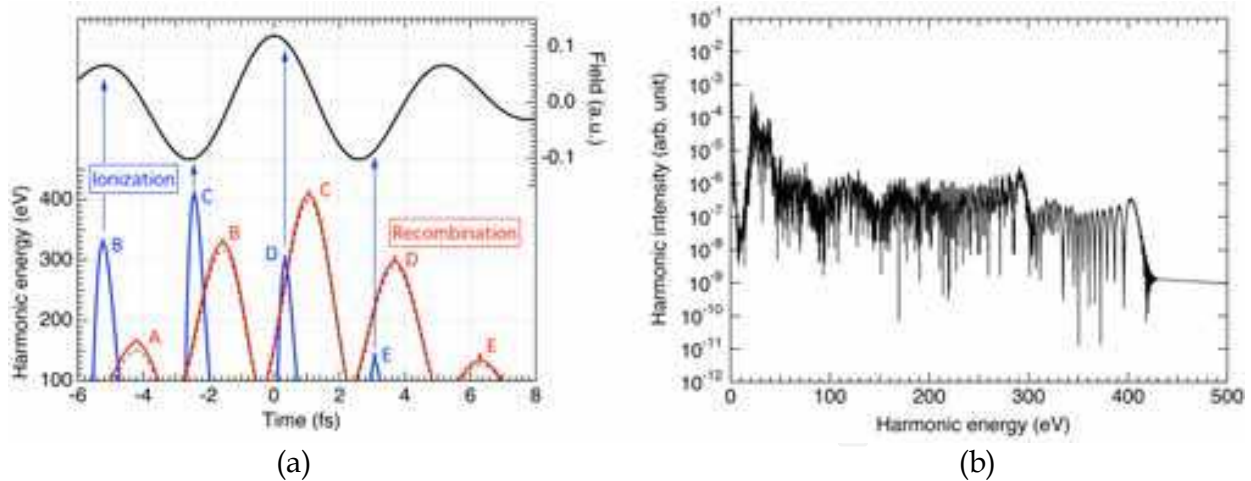


Fig. 7. (a) Real part of the recombination (red) and ionization times (blue) calculated from the saddle-point equations for the cos pulse. Each trajectory pair is labeled from A to E. The black dashed line is the recombination time from the three-step model. The electric field is also shown in black solid line. (b) Harmonic spectrum calculated with direct simulation of the TDSE.

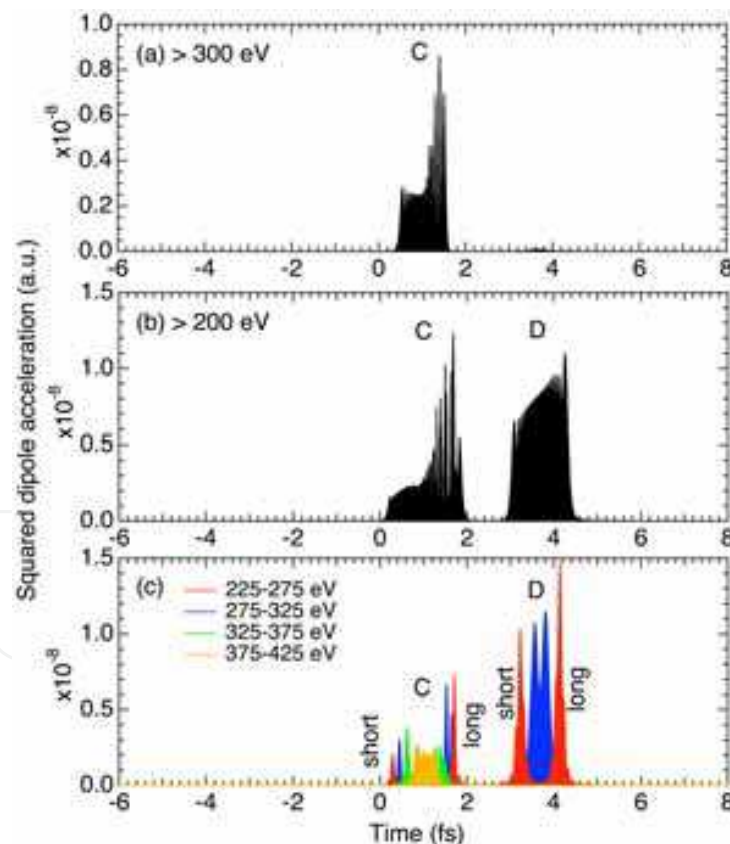


Fig. 8. Temporal profile of the TDSE-calculated squared dipole acceleration (SDA), proportional to the harmonic pulse intensity generated by the cos pulse, (a) at $\hbar\omega_h > 200\text{ eV}$, (b) at $\hbar\omega_h > 300\text{ eV}$, (c) for different energy ranges indicated in the panel. Labels C and D indicate corresponding trajectory pairs in Fig. 7 (a). Labels “short” and “long” indicate short and long trajectories, respectively.

pairs C and D. It is noteworthy that the trajectory pair C for the cutoff energy (~ 400 eV) is ionized *not* at the pulse peak but half cycle before it. Then the electron is accelerated efficiently by the subsequent pulse peak.

From the above consideration, and also remembering that harmonic emission occurs upon recombination, we can speculate the following:

- The harmonics above 200 eV consists of a train of two pulses at $t \approx 1$ (C) and 3.5 fs (D).
- By extracting the spectral component above 300 eV, one obtains an isolated attosecond pulse at $t \approx 1$ fs (C).
- The emission from the short (long) trajectories are positively (negatively) chirped, i.e., the higher the harmonic order, the later (the earlier) the emission time. The chirp leads to temporal broadening of the pulse.

These are indeed confirmed by the TDSE simulation results shown in Fig. 8, for which the calculated dipole acceleration is Fourier transformed, then filtered in energy, and transformed back into the time domain to yield the temporal structure of the pulse radiated from the atom.

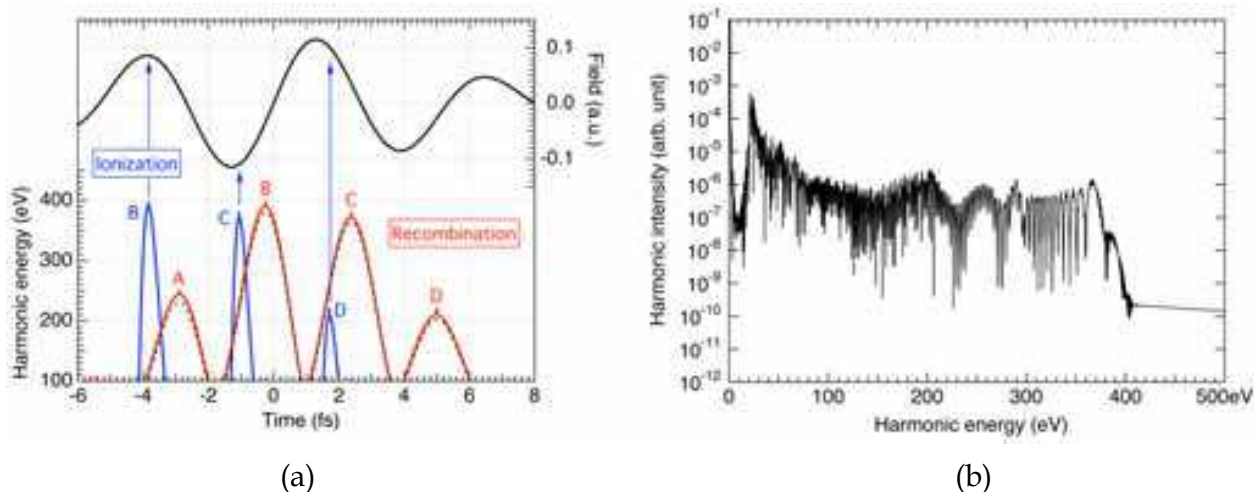


Fig. 9. (a) Real part of the recombination (red) and ionization times (blue) calculated from the saddle-point equations for the sin pulse. Each trajectory pair is labeled from A to D. The black dashed line is the recombination time from the three-step model. The electric field is also shown in black solid line. (b) Harmonic spectrum calculated with direct simulation of the TDSE.

3.2 Sin pulse

Let us now turn to the sin pulse. The harmonic spectrum (Fig. 9 (b)) has two-step cutoffs at 370 and 390 eV associated with trajectory pairs C and B (Fig. 9 (a)), respectively. The latter (B) is much less intense, since the laser field is weaker at the ionization time for pair B than for pair C as can be seen from Fig. 9 (a), leading to smaller tunneling ionization rate. The inspection of Fig. 9 (a), similar to what we did in the previous subsection, suggests that, noting field strength at the time of ionization,

- The harmonics above 100 eV consists of a train of two pulses at $t \approx 2.5$ (C) and 5 fs (D). The contribution from pairs A and B are negligible due to small ionization rate.
- By extracting the spectral component above 220 eV, one obtains an isolated attosecond pulse at $t \approx 2.5$ fs (C), *not* double pulse (B and C).

- As in the case of the cos pulse, the emission from the short (long) trajectories are positively (negatively) chirped. The chirp leads to temporal broadening of the pulse. The second point indicates that broader harmonic spectrum is available for isolated attosecond pulse generation with the sin pulse than with the cos pulse, implying potentially shorter soft x-ray pulse generation if the intrinsic chirp can be compensated (Sansone et al., 2006). It also follows from the comparison between Figs. 7 and 9 that for the case of few-cycle lasers high-harmonic generation is sensitive to the CEP (Baltuška et al., 2003). The examples discussed in this section stresses that the Lewenstein model and even the semiclassical three-step model, which is a good approximation to the former, are powerful tools to understand features in harmonic spectra and predict the temporal structure of generated pulse trains; the emission times in Figs. 8 and 10 could be predicted quantitatively well without TDSE simulations. One can calculate approximate harmonic spectra using the saddle-point analysis from Equation 21 or using the Gaussian model within the framework of SFA. On the other hand, the direct TDSE simulation is also a powerful tool to investigate quantitative details, especially the effects of excited levels and the atomic Coulomb potential (Schiessl et al., 2007; 2008; Ishikawa et al., 2009a).

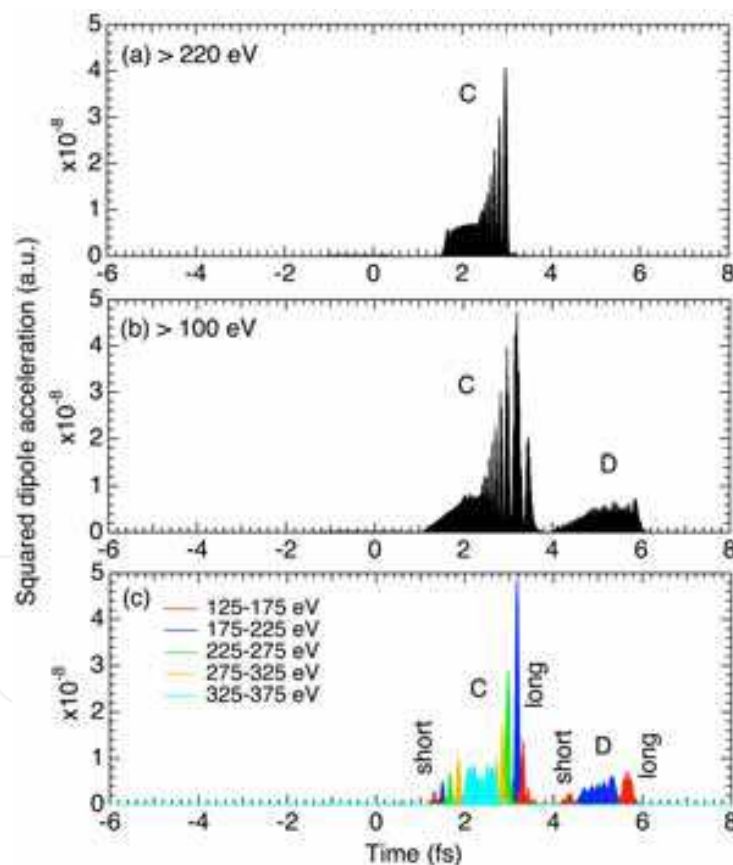


Fig. 10. Temporal profile of the TDSE-calculated squared dipole acceleration (SDA), proportional to the harmonic pulse intensity generated by the sin pulse, (a) at $\hbar\omega_i > 100$ eV, (b) at $\hbar\omega_i > 220$ eV, (c) for different energy ranges indicated in the panel. Labels C and D indicate corresponding trajectory pairs in Fig. 9 (a). Labels “short” and “long” indicate short and long trajectories, respectively.

4. High-harmonic generation controlled by an extreme ultraviolet pulse

In this section, we discuss how the addition of an intense extreme ultraviolet (xuv) pulse affects HHG (Ishikawa, 2003; 2004). Whereas the xuv pulse is not necessarily harmonics of the fundamental laser, let us first consider how a He⁺ ion behaves when subject to a fundamental laser pulse and an intense 27th or 13th harmonic pulse at the same time. Due to its high ionization potential (54.4 eV) He⁺ is not ionized by a single 27th and 13th harmonic photon. Here, we are interested especially in the effects of the simultaneous irradiation on harmonic photoemission and ionization. The fundamental laser pulse can hardly ionize He⁺ as we will see later. Although thanks to high ionization potential the harmonic spectrum from this ion would have higher cut-off energy than in the case of commonly used rare-gas atoms, the conversion efficiency is extremely low due to the small ionization probability. It is expected, however, that the addition of a Ti:Sapphire 27th or 13th harmonic facilitates ionization and photoemission, either through two-color frequency mixing or by assisting transition to the 2*p* or 2*s* levels. The direct numerical solution of the time-dependent Schrödinger equation shows in fact that the combination of fundamental laser and its 27th or 13th harmonic pulses dramatically enhance both high-order harmonic generation and ionization by many orders of magnitude.

To study the interaction of a He⁺ ion with a combined laser and xuv pulse, we solve the time-dependent Schrödinger equation in the length gauge,

$$i \frac{\partial \Phi(\mathbf{r}, t)}{\partial t} = \left[-\frac{1}{2} \nabla^2 - \frac{2}{r} - zE(t) \right] \Phi(\mathbf{r}, t), \quad (48)$$

where $E(t)$ is the electric field of the pulse. Here we have assumed that the field is linearly polarized in the z -direction. To prevent reflection of the wave function from the grid boundary, after each time step the wave function is multiplied by a $\cos^{1/8}$ mask function (Krause et al., 1992) that varies from 1 to 0 over a width of $2/9$ of the maximum radius at the outer radial boundary. The ionization yield is evaluated as the decrease of the norm of the wave function on the grid. The electric field $E(t)$ is assumed to be given by,

$$E(t) = F_F(t) \sin(\omega t) + F_H(t) \sin(n\omega t + \phi), \quad (49)$$

with $F_F(t)$ and $F_H(t)$ being the pulse envelope of the fundamental and harmonic pulse, respectively, chosen to be Gaussian with a duration (full width at half maximum) of 10 fs, ω the angular frequency of the fundamental pulse, n the harmonic order, and ϕ the relative phase. The fundamental wavelength is 800 nm unless otherwise stated. Since we have found that the results are not sensitive to ϕ , we set $\phi = 0$ hereafter.

4.1 HHG enhancement

In Fig. 11 we show the harmonic photoemission spectrum from He⁺ for the case of simultaneous fundamental and 27th harmonic (H27) irradiation. The peak fundamental intensity I_F is $3 \times 10^{14} \text{W/cm}^2$, and the peak H27 intensity I_{H27} is 10^{13}W/cm^2 . For comparison we also show the spectra obtained when only the fundamental pulse of the same intensity is applied to a He⁺ ion and a hydrogen atom. For the case of Fig. 11, the cutoff energy is calculated from Equation 1 to be 70 eV (H45) for a hydrogen atom and 111 eV (H73) for He⁺. The cutoff positions in Fig. 11 agree with these values, and harmonics of much higher orders

are generated from He^+ than from H. We note, however, that the harmonic intensity from He^+ when only the laser is applied is extremely low compared with the case of H. This is because the large ionization potential, though advantageous in terms of the cut-off energy, hinders ionization, the first step of the three-step model. The situation changes completely if the H27 pulse is simultaneously applied to He^+ . From Fig. 11 we can see that the conversion efficiency is enhanced by about seventeen orders of magnitude (Ishikawa, 2003; 2004). Moreover, the advantage of high cutoff is preserved. Figure 12 shows the harmonic

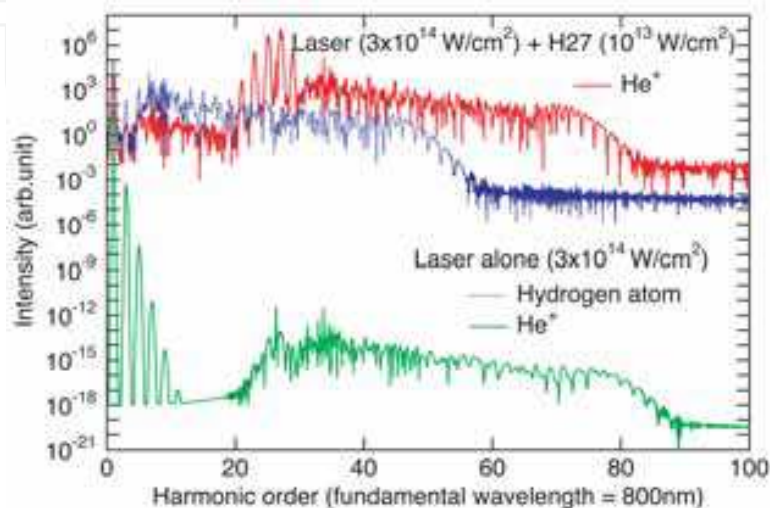


Fig. 11. Upper solid curve: harmonic spectrum from He^+ exposed to a Gaussian combined fundamental and its 27th harmonic pulse with a duration (FWHM) of 10 fs, the former with a peak intensity of $3 \times 10^{14} \text{W/cm}^2$ and the latter 10^{13}W/cm^2 . The fundamental wavelength is 800 nm. Lower solid and dotted curves: harmonic spectrum from He^+ and a hydrogen atom, respectively, exposed to the fundamental pulse alone. Nearly straight lines beyond the cut-off energy are due to numerical noise.

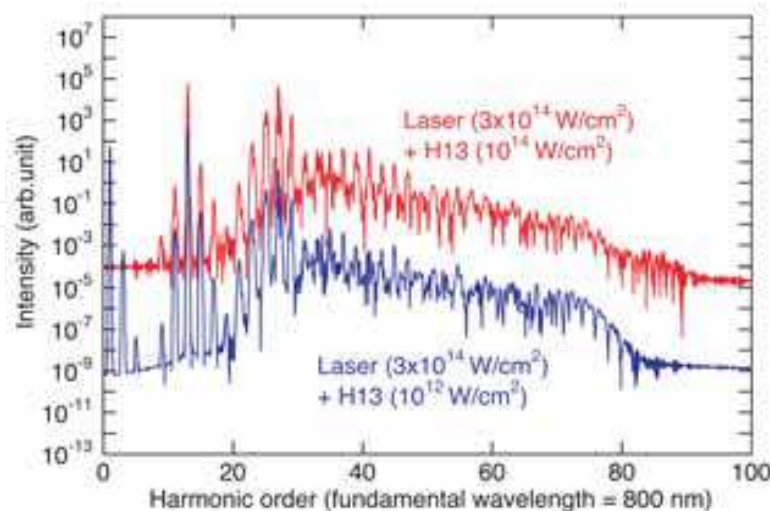


Fig. 12. Harmonic spectrum from He^+ exposed to a Gaussian combined fundamental and its 13th harmonic pulse with a duration (FWHM) of 10 fs, the former with a peak intensity of $3 \times 10^{14} \text{W/cm}^2$, and the latter 10^{14}W/cm^2 (upper curve) and 10^{12}W/cm^2 (lower curve). The fundamental wavelength is 800 nm. Note that the horizontal axis is of the same scale as in Fig. 11.

photoemission spectrum from He⁺ for the case of simultaneous fundamental and H13 irradiation. Again the harmonic intensity is enhanced by more than ten orders of magnitude compared to the case of the laser pulse alone. We have varied the fundamental wavelength between 750 and 850 nm and found similar enhancement over the entire range.

4.2 Enhancement mechanism

The effects found in Figs. 11 and 12 can be qualitatively understood as follows. The H27 photon energy (41.85 eV) is close to the 1s-2p transition energy of 40.8 eV, and the H13 photon (20.15 eV) is nearly two-photon resonant with the 1s-2s transition. Moreover, the 2p and 2s levels are broadened due to laser-induced dynamic Stark effect. As a consequence, the H27 and H13 promote transition to a virtual state near these levels. Depending on the laser wavelength, resonant excitation of 2s or 2p levels, in which fundamental photons may be involved in addition to harmonic photons, also takes place. In fact, the 2s level is excited through two-color two-photon transition for the case of Fig. 11 at $\lambda_F = 800$ nm, as we will see below in Fig. 15, and about 8% of electron population is left in the 2s level after the pulse. Since this level lies only 13.6 eV below the ionization threshold, the electron can now be lifted to the continuum by the fundamental laser pulse much more easily and subsequently emit a harmonic photon upon recombination. Thus the HHG efficiency is largely increased. We have found that the harmonic spectrum from the superposition of the 1s (92%) and 2s (8%) states subject to the laser pulse alone is strikingly similar to the one in Fig. 11. Hence the effect may also be interpreted as harmonic generation from a coherent superposition of states (Watson et al., 1996). On the other hand, at a different fundamental wavelength, e.g., at $\lambda_F = 785$ nm, there is practically no real excitation. Nevertheless the photoemission enhancement (not shown) is still dramatic. This indicates that fine tuning of the xuv pulse to the resonance with an excited state is *not* necessary for the HHG enhancement. In this case, the H27 pulse promotes transition to a virtual state near the 2p level. Again, the electron can easily be lifted from this state to the continuum by the fundamental pulse, and the HHG efficiency is largely augmented. This may also be viewed as two-color frequency mixing enhanced by the presence of a near-resonant intermediate level. In general, both mechanisms of harmonic generation from a coherent superposition of states and two-color frequency mixing coexist, and their relative importance depends on fundamental wavelength. A similar discussion applies to the case of the H13 addition. The comparison of the two curves in Fig. 12 reveals that the harmonic spectrum is proportional to I_{H13}^2 , where I_{H13} denotes the H13 peak intensity. We have also confirmed that the photoemission intensity is proportional to I_{H27} for the case of H27. These observations are compatible with the discussion above.

4.3 Ionization enhancement

Let us now examine ionization probability. Table 1 summarizes the He²⁺ yield for each case of the fundamental pulse alone, the harmonic pulse alone, and the combined pulse. As can be expected from the discussion in the preceding subsection, the ionization probability by the combined pulse is by many orders of magnitude higher than that by the fundamental laser pulse alone. Especially dramatic enhancement is found in the case of the combined fundamental and H27 pulses: the He²⁺ yield is increased by orders of magnitude also with respect to the case of the H27 irradiation alone. This reflects the fact that field ionization from the 2s state by the fundamental pulse is much more efficient than two-photon

ionization from the ground state by the H27 pulse. In Fig. 13, we plot the He^{2+} yield as a function of I_{H27} for a fixed fundamental intensity of $3 \times 10^{14} \text{W/cm}^2$. The ionization probability is linear in I_{H27} except for the saturation at $I_{\text{H27}} > 10^{13} \text{W/cm}^2$. This is compatible with our view that an H27 photon promotes $1s$ - $2s$ two-color two-photon transition, followed by field ionization.

I_F (W/cm^2)	I_{H27} (W/cm^2)	I_{H13} (W/cm^2)	He^{2+} yield
3×10^{14}	—	—	2.29×10^{-15}
—	10^{13}	—	4.79×10^{-6}
3×10^{14}	10^{13}	—	0.173
—	—	10^{14}	1.25×10^{-4}
3×10^{14}	—	10^{14}	2.04×10^{-4}

Table 1. The He^{2+} yield for various combinations of a Gaussian fundamental and its 27th or 13th harmonic pulses with a duration (FWHM) of 10 fs and a peak intensity listed in the table. $\lambda_F = 800 \text{ nm}$.

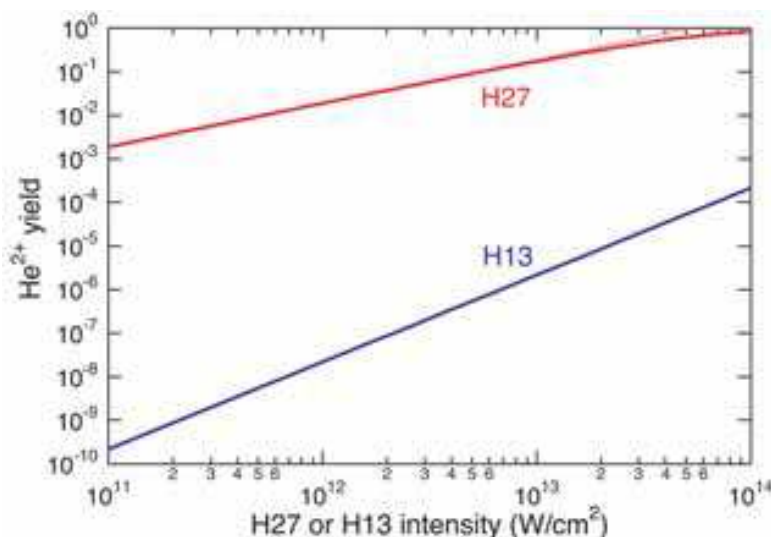


Fig. 13. The He^{2+} yield as a function of peak intensity of the 27th (upper curve) and 13th (lower curve) harmonic pulse when He^+ is exposed to a Gaussian combined fundamental and its 27th harmonic pulse with a duration (FWHM) of 10 fs. The wavelength λ_F and the peak intensity I_F of the fundamental pulse are 800 nm and $3 \times 10^{14} \text{W/cm}^2$, respectively.

Figure 14 shows the dependence of the He^{2+} yield on the peak intensity I_F of the fundamental pulse. Surprisingly, the yield is not monotonically increasing in I_F : ionization is decreased with an increasing laser intensity at $I_F > 3 \times 10^{14} \text{W/cm}^2$ in the presence of the H27 pulse and at $2 \times 10^{14} < I_F < 4 \times 10^{14} \text{W/cm}^2$ in the presence of the H13 pulse. In order to clarify the origin of this counter-intuitive behavior, we have calculated the dependence of the He^{2+} yield on the fundamental wavelength λ_F for different values of fundamental intensity. The results are shown in Fig. 15 for the cases of $I_{\text{H27}} = 10^{13} \text{W/cm}^2$ and $I_F = 5 \times 10^{13}, 8 \times 10^{13}, 3 \times 10^{14}, 5 \times 10^{14}, 10^{15} \text{W/cm}^2$. The curve for $I_F = 5 \times 10^{13} \text{W/cm}^2$ peaks around $\lambda_F = 820 \text{ nm}$, for which the H27 photon energy is exactly resonant with the $1s$ - $2p$ transition. At $I_F = 8 \times 10^{13} \text{W/cm}^2$ we can see a second peak around $\lambda_F = 793 \text{ nm}$, for which $26\hbar\omega (= 27\hbar\omega - \hbar\omega)$ coincides with the $1s$ - $2s$ transition energy. This indicates that at this wavelength the $2s$ level is resonantly populated through two-color two-photon excitation, as we alluded earlier.

With increasing laser intensity, the peaks are shifted to longer wavelengths due to the laser-induced dynamic Stark effect, and at $I_F = 3 \times 10^{14} \text{ W/cm}^2$ the second peak, now higher than the first one, is located around 800 nm, which leads to high ionization yield at this wavelength. At $I_F = 3 \times 10^{14} \text{ W/cm}^2$, we can also see a third peak around $\lambda_F = 770 \text{ nm}$ corresponding to two-color $2p$ excitation involving one H27 and two fundamental photons. The dynamic Stark effect induces not only the peak shift but also the peak broadening, which results in the decrease of peak heights at higher fundamental intensity, leading to the decrease of the ionization yield at $I_F > 3 \times 10^{14} \text{ W/cm}^2$ in Fig. 14. Thus, the role of the

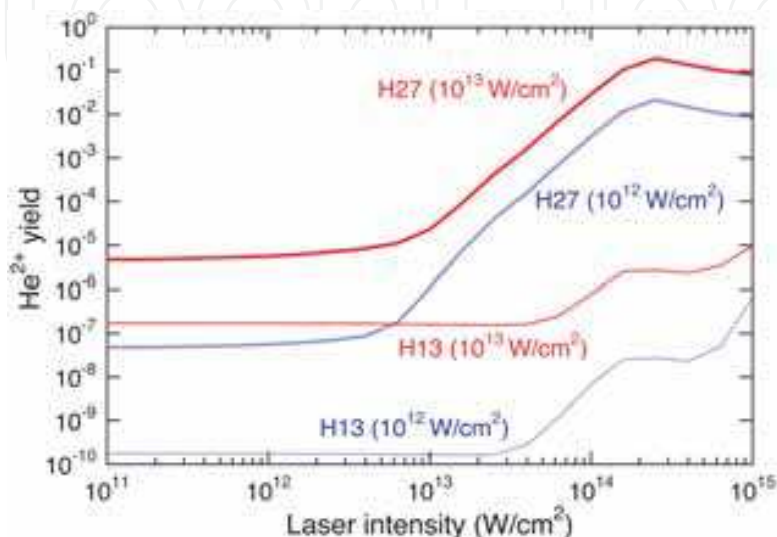


Fig. 14. The He^{2+} yield as a function of peak intensity I_F of the fundamental laser pulse when He^+ is exposed to a Gaussian combined fundamental and its 27th or 13th harmonic pulse with a duration (FWHM) of 10 fs. The fundamental wavelength λ_F is 800 nm. The peak intensity of each harmonic pulse is indicated in the figure along with its order.

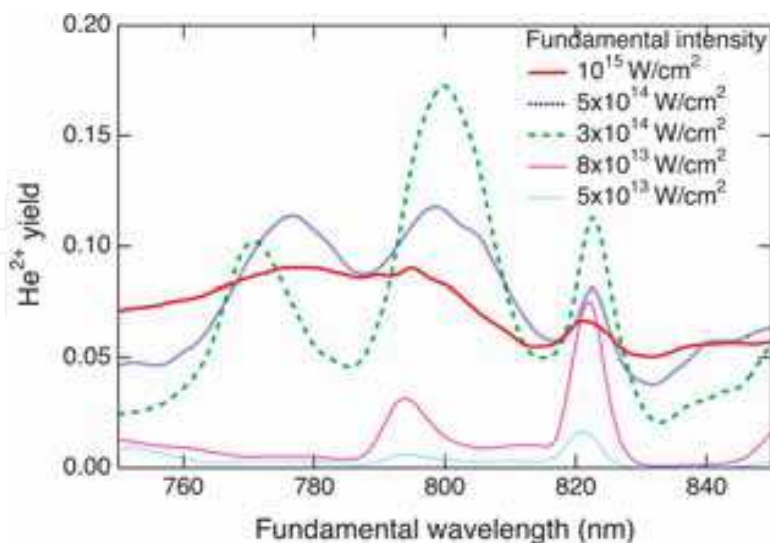


Fig. 15. The He^{2+} yield as a function of fundamental wavelength when He^+ is exposed to a Gaussian combined fundamental and its 27th harmonic pulse with a duration (FWHM) of 10 fs. The peak intensity I_{H27} of the 27th harmonic pulse is fixed at 10^{13} W/cm^2 , and we plot the results for five different values of fundamental peak intensity I_F indicated in the figure. Note that the wavelength of the 27th harmonic varies with that of the fundamental pulse.

fundamental laser pulse is three-fold: to lift the electron in an excited (real or virtual) level to the continuum through optical-field ionization, to assist $1s$ - $2s$, $2p$ transitions through two-color excitation, and to induce dynamic Stark shift and broadening. The interplay of these three leads to a complicated behavior seen in Fig. 14.

4.4 Remarks

The mechanism of the HHG enhancement discussed above is that the xuv addition increases the field ionization rate by promoting transition to (real or virtual) excited states, from which ionization is much easier than from the ground state. Hence, the enhancement is effective *only when the ionization rate by the fundamental pulse alone is not high enough*. If HHG is already optimized by a sufficiently intense laser pulse, the xuv addition does not increase the HHG yield significantly.

Although the cases involving resonant transitions are highlighted above, the resonance with an excited state is *not* necessary for the enhancement. Figure 16 shows the harmonic spectra from He for $\lambda = 1600\text{nm}$ with and without the XUV field ($\hbar\omega_X = 17.05\text{eV}$). For the case of the driving laser alone with a peak intensity I of $1.6 \times 10^{14}\text{W/cm}^2$ (blue curve), the ionization yield Y_I is very low ($1.7 \times 10^{-5}\%$). The addition of the xuv pulse with an intensity of $2.3 \times 10^{11}\text{W/cm}^2$ increases Y_I to 0.31% and enhances the harmonic yield accordingly (red curve). In this case, the xuv photon energy is not resonant with transition to excited states. Nevertheless, the HHG yield is enhanced by orders of magnitude. The dramatic enhancement effect has been experimentally demonstrated by the use of mixed gases (Takahashi et al., 2007); also in this experiment, the booster xuv pulse (harmonics from Xe) was non-resonant with the target atom (He).

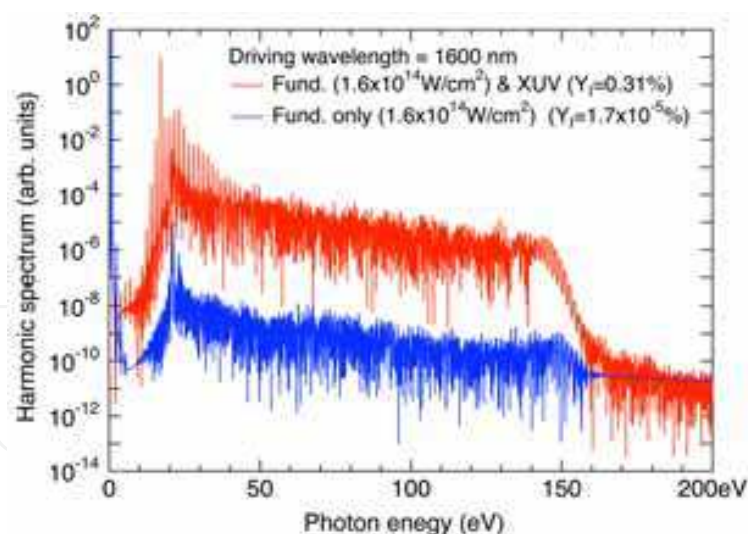


Fig. 16. Upper curve: harmonic spectrum from He exposed to a 35 fs Gaussian combined driving and XUV pulse ($\hbar\omega_X = 17.05\text{eV}$), the former ($\lambda = 1600\text{ nm}$) with a peak intensity of $1.6 \times 10^{14}\text{W/cm}^2$ and the latter $2.3 \times 10^{11}\text{W/cm}^2$. Lower curve: harmonic spectra for the cases of the driving pulse alone, with an intensity of $1.6 \times 10^{14}\text{W/cm}^2$.

4.5 Single attosecond pulse generation using the enhancement effect

The progress in the high-harmonic generation (HHG) technique has raised significant interest in the generation of attosecond pulses. As we have seen in Subsec. 2.1, the

photoemission process is repeated every half-cycle of the laser optical field and produces an attosecond pulse train (Fig. 3). On the other hand, a single attosecond pulse (SAP), in particular, is critical for the study of the electron dynamics inside atoms (Krausz & Ivanov, 2009). If the driving laser pulse is sufficiently short that the effective HHG takes place only within one half-cycle, the cut-off region of the spectrum may become a continuum, corresponding to a single recollision (Figs. 8 and 10). The first SAPs (Baltuška et al., 2003) were obtained on this basis. Isolated attosecond pulses have also been realized by other methods such as *ionization shutter* (Sekikawa et al., 2004) and *polarization gate* (Corkum et al., 1994; Sansone et al., 2006), and *two-color scheme* (Pfeifer et al., 2006) has also been proposed. The enhancement effect discussed in the preceding subsections provides a means to control HHG and new physical insights (Schafer et al., 2004; Ishikawa et al., 2009b). As an example, in this subsection, we present an alternative method of SAP generation using multi-cycle laser pulses, called *attosecond enhancement gate for isolated pulse generation (AEGIS)* (Ishikawa et al., 2007). Let us first describe AEGIS qualitatively (Figs. 17(a) and 18(a)). The underlying mechanism of the HHG enhancement by the addition of xuv pulses is that the seed pulse induces transition to real or virtual excited levels, facilitating optical-field ionization, the

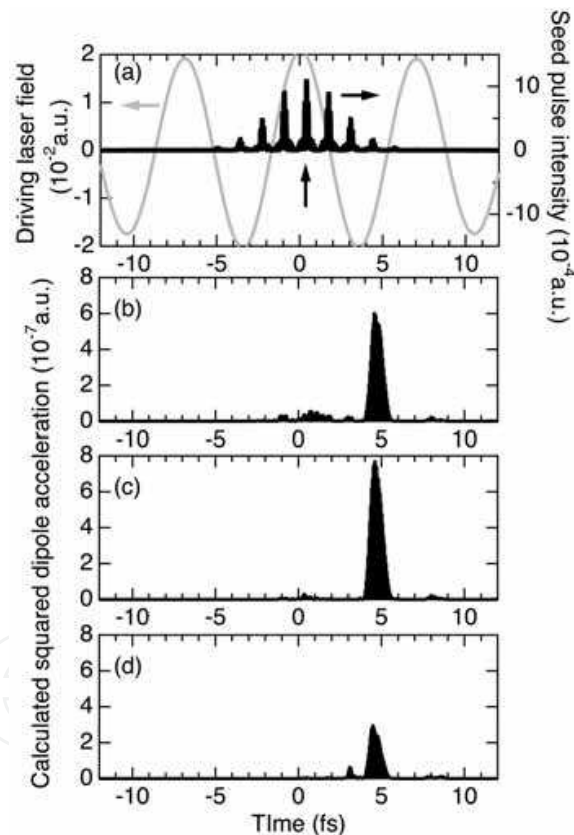


Fig. 17. Soft-x-ray pulse generation by the combination of $\lambda_d = 2.1\mu\text{m}$ and $\lambda_{sf} = 800\text{nm}$. (a) temporal profile of the seed harmonic pulse intensity (black, right axis) with a global pulse width of 5 fs and the driving laser field (gray, left axis) with a pulse duration of 30 fs. The vertical arrow indicates the pulse expected to act as a gate to enhance HHG. (b) temporal profile of the calculated squared dipole acceleration (SDA), proportional to the generated pulse intensity, around 30 nm wavelength. (c) SDA when the seed pulse train has a global pulse width of 3 fs. (d) SDA when, in addition, the delay of the seed pulse train is a quarter cycle of the driving field.

first step of the three-step model. When the seed is composed of a train of attosecond pulses, this can be viewed as repeated attosecond enhancement gates. Let us consider that the fundamental pulse generating the seed harmonic pulse, referred to as the *seed fundamental* pulse hereafter, and the driving laser pulse which will be combined with the seed pulse have different wavelengths. For example, when the seed fundamental wavelength $\lambda_{s,f}$ and the driving wavelength λ_d are 800 nm and $2.1\mu\text{m}$, respectively, a seed harmonic pulse train even composed of several attosecond pulses repeated every 1.33 fs is confined within one cycle (7 fs) of the driving laser, as is schematically shown in Fig. 17 (a). Hence, we would expect that the enhanced harmonic emission forms a SAP. When $\lambda_{s,f} = 2.1\mu\text{m}$ and $\lambda_d = 800\text{nm}$, conversely, seed harmonic pulses are separated by 3.5 fs, which is longer than the driving laser cycle (2.67 fs). If the seed harmonic pulse train and the driving pulse are superposed as shown in Fig. 18(a), only the central pulse would contribute to HHG in the cutoff region, resulting in SAP generation.

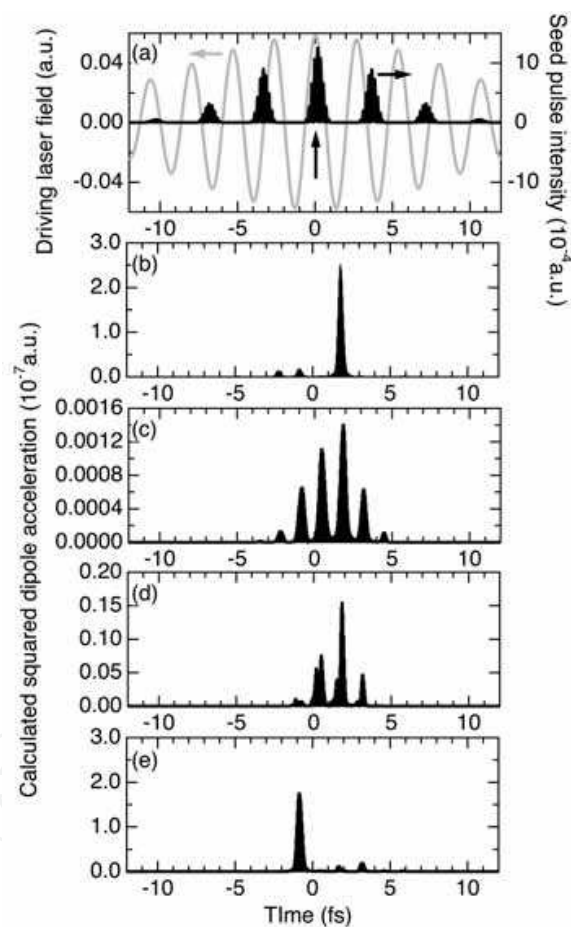


Fig. 18. Soft-x-ray pulse generation by the combination of $\lambda_d = 800\text{nm}$ and $\lambda_{s,f} = 2.1\mu\text{m}$. (a) temporal profile of the seed harmonic pulse intensity (black, right axis) with a global pulse width of 10 fs and the driving laser field (gray, left axis) with a pulse duration of 15 fs. The vertical arrow indicates the pulse expected to act as a gate to enhance HHG. (b) temporal profile of the calculated SDA, proportional to the generated pulse intensity, around 24 nm wavelength. (c) SDA in the absence of the seed pulse (d) SDA when $\lambda_{s,f} = 800\text{nm}$ (e) SDA when the delay of the seed pulse train ($\lambda_{s,f} = 2.1\mu\text{m}$) is a quarter cycle of the driving field.

Furthermore, the kinetic energy of the recombining electron and, thus, the emitted photon energy in the three-step model depends on the electron's time of release, and that, in particular, an electron ionized by tunneling at $\omega t = \phi_c, \phi_c + 180^\circ, \dots$ ($\phi_c \approx 17^\circ$), around the pulse peak contributes to cut-off emission. Therefore, when only one pulse of the seed pulse train is adjusted to satisfy this relation, marked by vertical arrows in Figs. 17(a) and 18(a), only that pulse could contribute to harmonic emission in the cut-off region, which would further favor SAP generation, even though the driving pulse is relatively long and the seed contains multiple pulses.

We now confirm this qualitative idea, using direct numerical solution of the time-dependent Schrödinger equation. The harmonic spectrum is calculated by Fourier transforming the dipole acceleration, then high-pass filtered as is done in experiments with multilayer mirrors, and transformed back into the time domain to yield the temporal structure of the pulse radiated from the atom.

Let us first consider the case where $\lambda_s = 800\text{nm}$ and $\lambda_d = 2.1\mu\text{m}$. Figure 17(a) displays the seed harmonic pulse train used in the present simulation. The pulse train

$$E_s(t) = E_{s0}(t - \phi_c / \omega_d) \sum_{q(\text{odd})=11}^{19} f_q \cos[q\omega_s(t - \phi_c / \omega_d)], \quad (50)$$

is composed of the 11th to 19th harmonics. We use experimentally observed values (Takahashi et al., 2002) for the harmonic mixing ratio $(f_{11}^2, f_{13}^2, f_{15}^2, f_{17}^2, f_{19}^2) = (0.50, 0.34, 0.07, 0.04, 0.05)$, and the common amplitude envelope $E_{s0}(t - \phi_c / \omega_d)$ is assumed to be of a Gaussian temporal profile centered at $t = \phi_c / \omega_d$ with a full width at half maximum (FWHM) of 5 fs, referred to as a global pulse width hereafter. The sum of peak intensity of each component is $10^{13}\text{W}/\text{cm}^2$. Such a train of ca. 7 pulses would typically be generated by applying a Ti:Sapphire laser pulse of a duration ≈ 15 fs to a Xe gas, and even higher intensity has experimentally been realized using 20 mJ laser pulses (Takahashi et al., 2002). The intensity of the resulting harmonic pulse is proportional to that of the seed harmonic pulse, but its relative temporal structure is not affected by the latter. The driving pulse $E_d(t)$, also shown in Fig. 17(a), is assumed to have a Gaussian temporal intensity profile centered at $t = 0$ with a FWHM of 30 fs. The peak intensity I_d is $1.5 \times 10^{13}\text{W}/\text{cm}^2$. Figure 17(b) presents the calculated squared dipole acceleration (SDA), which is proportional to the intensity of the pulse radiated from a Ne atom subject to the seed harmonic and the driving pulses simultaneously, as would be obtained after reflected by a multilayer X-ray mirror whose reflectivity peaks in the cut-off region around 30 nm (H67-H75). As we have expected, we can see that only the central pulse in the seed (Fig. 17(a)) acts as a gate for dramatic enhancement of HHG in the cut-off region and that a practically single pulse with a FWHM of 800 as is obtained, even though small satellite pulses are present. If we use a seed pulse train with a 3 fs global pulse width, composed of ca. 5 pulses, we can suppress the satellite pulses, as is shown in Fig. 17(c). It should be noted that the driving pulse alone would generate virtually no harmonics for this driving intensity. This indicates that even if the driving laser is not sufficiently intense for HHG, the combination with a seed pulse can serve as efficient means to generate a harmonic single pulse. If we use a higher driving intensity, on the other hand, we obtain a single pulse of shorter wavelength and duration; for the case of $I_d = 10^{14}\text{W}/\text{cm}^2$, e.g., a 580 as single pulse would be obtained around 10 nm wavelength. Although the seed contains harmonic components (H15-H19) which may

induce direct ionization, the obtained pulses are mainly due to H11 and H13 with a photon energy below the ionization threshold. We have confirmed this by simulations excluding H15-H19.

Let us next turn to the case where $\lambda_s = 2.1\mu\text{m}$ and $\lambda_d = 800\text{nm}$. Figure 18(a) displays the seed harmonic pulse train,

$$E_s(t) = E_{s0}(t - \phi_c / \omega_d) \sum_{q(\text{odd})=15}^{23} f_q \cos[q\omega_{sf}(t - \phi_c / \omega_d)], \quad (51)$$

containing ca. 5 pulses, composed of the 15th to 23rd harmonics. The harmonic mixing ratio is $(f_{15}^2, f_{17}^2, f_{19}^2, f_{21}^2, f_{23}^2) = (0.0625, 0.25, 0.375, 0.25, 0.0625)$, and the common amplitude envelope with a FWHM of 10 fs peaks at $t = \phi_c / \omega_d$. The sum of peak intensity of each component is $10^{13}\text{W}/\text{cm}^2$. The driving pulse $E_d(t)$, also shown in Fig. 18(a), is assumed to have a FWHM of 15 fs and a peak intensity I_d of $1.2 \times 10^{14}\text{W}/\text{cm}^2$. Figure 18(b) presents the calculated SDA, as would be obtained after reflected by a multilayer X-ray mirror whose reflectivity peaks in the cut-off region around 24 nm (H31-H35). The result, containing ca. 4 pulses, for the case of the driving pulse alone is shown in Fig. 18(c). From Fig. 18(b), we can see that only the middle pulse in the seed significantly boosts HHG in the cut-off region, thus leading to a single pulse with a duration of 350 as. This is shorter than in Fig. 17, probably because the phase range of the driving field relevant with the cut-off region translates to a shorter time interval due to a shorter driving wavelength. The small satellite pulses are further suppressed if the seed pulse is composed of a larger number of orders, for which each pulse in the train becomes shorter.

5. References

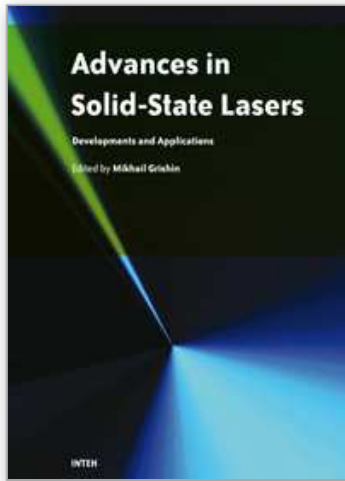
- Baltuška, A., Udem, Th., Uiberacker, M., Hentschel, M., Goulielmakis, E., Gohle, Ch., Holzwarth, R., Yakovlev, V. S., Scrinzi, A., Hänsch, T.W. & Krausz, F. (2003). Attosecond control of electronic processes by intense light fields. *Nature* 421(6923): 611-615.
- Bauer, D. & Koval, P. (2006). Qprop: A Schrödinger-solver for intense laser-atom interaction. *Comp. Phys. Comm.* 174(5): 396-421.
- Corkum, P. B. (1993). Plasma perspective on strong-field multiphoton ionization. *Phys. Rev. Lett.* 71(13): 1994-1997.
- Corkum, P. B., Burnett, N. H. & Ivanov, M. Y. (1994). Subfemtosecond pulses. *Opt. Lett.* 19(22): 1870-1872.
- Ishikawa, K. (2003). Photoemission and ionization of He^+ under simultaneous irradiation of fundamental laser and high-order harmonic pulses. *Phys. Rev. Lett.* 91(4): 043002.
- Ishikawa, K. L. (2004). Efficient photoemission and ionization of He^+ by a combined fundamental laser and high-order harmonic pulse *Phys. Rev. A* 70(1): 013412.
- Ishikawa, K. L., Takahashi, E. J. & Midorikawa, K. (2007). Single-attosecond pulse generation using a seed harmonic pulse train. *Phys. Rev. A* 75(2): 021801(R).
- Ishikawa, K. L., Schiessl, K., Persson, E. & Burgdörfer, J. (2009). Fine-scale oscillations in the wavelength and intensity dependence of high-order harmonic generation: Connection with channel closings. *Phys. Rev. A* 79(3): 033411.

- Ishikawa, K. L., Takahashi, E. J. & Midorikawa, K. (2009). Wavelength dependence of high-order harmonic generation with independently controlled ionization and ponderomotive energy. *Phys. Rev. A* 80(1): 011807.
- Koonin, S. E., Davies, K. T. R., Maruhn-Rezwani, V., Feldmeier, H., Krieger, S. J. & Negele, J. W. (1977). Time-dependent Hartree-Fock calculations for $^{16}\text{O} + ^{16}\text{O}$ and $^{40}\text{Ca} + ^{40}\text{Ca}$ reactions. *Phys. Rev. C* 15(4): 1359–1374.
- Krause, J. L., Schafer, K. J. & Kulander, K. C. (1992). High-order harmonic generation from atoms and ions in the high intensity regime. *Phys. Rev. Lett.* 68(24): 3535–3538.
- Krausz, F. & Krausz, F. (2009). Attosecond physics. *Rev. Mod. Phys.* 81(1): 163–234.
- Kulander, K. C., Schafer, K. J. & Krause, J. L. (1992). Time-dependent studies of multiphoton processes, In: *Atoms in intense laser fields*, Gavrilu, M. (Ed.), 247–300, Academic Press, ISBN 0-12-003901-X, New York.
- Lewenstein, M., Balcou, Ph., Ivanov, M. Yu., L’Huillier, A., & Corkum, P. B. (1994). Theory of high-harmonic generation by low-frequency laser fields. *Phys. Rev. A* 49(3): 2117–2132.
- Muller, H. G. & Kooiman, F. C (1998). Bunching and focusing of tunneling wave packets in enhancement of high-order above-threshold ionization. *Phys. Rev. Lett.* 81(6): 1207–1210.
- Muller, H. G. (1999). An efficient propagation scheme for the time-dependent Schrödinger equation in the velocity gauge. *Laser Phys.* 9(1): 138–148.
- Nabekawa, Y., Shimizu, T., Okino, T., Furusawa, K., Hasegawa, H., Yamanouchi, K., & Midorikawa (2006). Conclusive evidence of an attosecond pulse train observed with the mode-resolved autocorrelation technique. *Phys. Rev. Lett.* 96(8): 083901.
- Pfeifer, T., Gallmann, L., Abel, M. J., Neumark, D. M. & Leone, S. R. (2006). Single attosecond pulse generation in the multicycle-driver regime by adding a weak second-harmonic field. *Opt. Lett.* 31(7): 975–977.
- Salières, P., Carré, B., Le Déroff, L., Grasbon, F., Paulus, G. G., Walther, H., Kopold, R., Becker, W., Milošević, D. B., Sanpera, A. & Lewenstein, M. (2001). Feynman’s path-integral approach for intense-laser-atom interactions. *Science* 292(5518): 902–905.
- Sansone, G., Benedetti, E., Calegari, F., Vozzi, C., Avaldi, L., Flammini, R., Poletto, L., Villorosi, P., Altucci, C., Velotta, R., Stagira, S., De Silvestri, S. & Nisoli, M. (2006). Isolated single-cycle attosecond pulses. *Science* 314(5798): 443–446.
- Schafer, K. J., Yang, B., DiMauro, L. F. & Kulander, K. C. (1993). Above threshold ionization beyond the high harmonic cutoff. *Phys. Rev. Lett.* 70(11): 1599–1602.
- Schafer, K. J., Gaarde, M. B., Heinrich, A., Biegert, J. & Keller, U. (2004). Strong field quantum path control using attosecond pulse trains. *Phys. Rev. Lett.* 92(2): 023003.
- Schiessl, K., Ishikawa, K. L., Persson, E. & Burgdörfer, J. (2007). Quantum path interference in the wavelength dependence of high-harmonic generation. *Phys. Rev. Lett.* 99(25): 253903.
- Schiessl, K., Ishikawa, K. L., Persson, E. & Burgdörfer, J. (2008). Wavelength dependence of high-harmonic generation from ultrashort pulses. *J. Mod. Opt.* 55(16): 2617–2630.
- Sekikawa, T., Kosuge, A., Kanai, T. & Watanabe, S. (2004). Nonlinear optics in the extreme ultraviolet. *Nature* 432(7017): 605–608.
- Takahashi, E. J., Nabekawa, Y., Otsuka, T., Obara, M. & Midorikawa, K. (2002) Generation of highly coherent submicrojoule soft x rays by high-order harmonics. *Phys. Rev. A* 66(2): 021802(R).

- Takahashi, E. J., Kanai, T., Ishikawa, K. L., Nabekawa, Y. & Midorikawa, K. (2007). Dramatic enhancement of high-order harmonic generation. *Phys. Rev. Lett.* 99(5): 053904.
- Tong, X.-M. & Chu, S.-I (1997). Theoretical study of multiple high-order harmonic generation by intense ultrashort pulsed laser fields: A new generalized pseudospectral timedependent method. *Chem. Phys.* 217(2-3): 119-130.
- Watson, J. B., Sanpera, A., Chen, X. & Burnett, K. (1996). Harmonic generation from a coherent superposition of states. *Phys. Rev. A* 53(4): R1962-R1965.

IntechOpen

IntechOpen



Advances in Solid State Lasers Development and Applications

Edited by Mikhail Grishin

ISBN 978-953-7619-80-0

Hard cover, 630 pages

Publisher InTech

Published online 01, February, 2010

Published in print edition February, 2010

Invention of the solid-state laser has initiated the beginning of the laser era. Performance of solid-state lasers improved amazingly during five decades. Nowadays, solid-state lasers remain one of the most rapidly developing branches of laser science and become an increasingly important tool for modern technology. This book represents a selection of chapters exhibiting various investigation directions in the field of solid-state lasers and the cutting edge of related applications. The materials are contributed by leading researchers and each chapter represents a comprehensive study reflecting advances in modern laser physics. Considered topics are intended to meet the needs of both specialists in laser system design and those who use laser techniques in fundamental science and applied research. This book is the result of efforts of experts from different countries. I would like to acknowledge the authors for their contribution to the book. I also wish to acknowledge Vedran Kordic for indispensable technical assistance in the book preparation and publishing.

How to reference

In order to correctly reference this scholarly work, feel free to copy and paste the following:

Kenichi L. Ishikawa (2010). High-Harmonic Generation, *Advances in Solid State Lasers Development and Applications*, Mikhail Grishin (Ed.), ISBN: 978-953-7619-80-0, InTech, Available from:

<http://www.intechopen.com/books/advances-in-solid-state-lasers-development-and-applications/high-harmonic-generation>

INTECH
open science | open minds

InTech Europe

University Campus STeP Ri
Slavka Krautzeka 83/A
51000 Rijeka, Croatia
Phone: +385 (51) 770 447
Fax: +385 (51) 686 166
www.intechopen.com

InTech China

Unit 405, Office Block, Hotel Equatorial Shanghai
No.65, Yan An Road (West), Shanghai, 200040, China
中国上海市延安西路65号上海国际贵都大饭店办公楼405单元
Phone: +86-21-62489820
Fax: +86-21-62489821

© 2010 The Author(s). Licensee IntechOpen. This chapter is distributed under the terms of the [Creative Commons Attribution-NonCommercial-ShareAlike-3.0 License](#), which permits use, distribution and reproduction for non-commercial purposes, provided the original is properly cited and derivative works building on this content are distributed under the same license.

IntechOpen

IntechOpen